

DOI: [10.29026/oes.2023.220023](https://doi.org/10.29026/oes.2023.220023)

# Deep learning assisted variational Hilbert quantitative phase imaging

Zhuoshi Li<sup>1,2,3</sup>, Jiasong Sun<sup>1,2,3</sup>, Yao Fan<sup>1,2,3</sup>, Yanbo Jin<sup>1,2,3</sup>, Qian Shen<sup>1,2,3</sup>,  
Maciej Trusiak<sup>4</sup>, Maria Cywińska<sup>4</sup>, Peng Gao<sup>5\*</sup>, Qian Chen<sup>3\*</sup> and  
Chao Zuo<sup>1,2,3\*</sup>

<sup>1</sup>Smart Computational Imaging Laboratory (SCILab), School of Electronic and Optical Engineering, Nanjing University of Science and Technology, Nanjing 210094, China; <sup>2</sup>Smart Computational Imaging Research Institute (SCIRI) of Nanjing University of Science and Technology, Nanjing 210094, China; <sup>3</sup>Jiangsu Key Laboratory of Spectral Imaging and Intelligent Sense, Nanjing 210094, China; <sup>4</sup>Institute of Micromechanics and Photonics, Warsaw University of Technology, 8 Sw. A. Boboli St., Warsaw 02-525, Poland; <sup>5</sup>School of Physics, Xidian University, Xi'an 710126, China.

\*Correspondence: P Gao, E-mail: [peng.gao@xidian.edu.cn](mailto:peng.gao@xidian.edu.cn); Q Chen, E-mail: [chenqian@njust.edu.cn](mailto:chenqian@njust.edu.cn); C Zuo, E-mail: [zuochoao@njust.edu.cn](mailto:zuochoao@njust.edu.cn)

## This file includes:

[Section 1: Low-carrier frequency hologram simulation and ground-truth acquisition](#)

[Section 2: Collection of training data from slightly off-axis DH system](#)

[Section 3: Discussion of FT phase recovery with different window sizes](#)

[Section 4: DL-noPhy network description](#)

[Section 5: Supplementary experiment results based on FT and VHQPPI methods for living cells](#)

Supplementary information for this paper is available at <https://doi.org/10.29026/oes.2023.220023>



**Open Access** This article is licensed under a Creative Commons Attribution 4.0 International License.

To view a copy of this license, visit <http://creativecommons.org/licenses/by/4.0/>.

© The Author(s) 2023. Published by Institute of Optics and Electronics, Chinese Academy of Sciences.

This document provides supplementary information to “Deep learning assisted variational Hilbert quantitative phase imaging”. We describe the process of low-carrier frequency hologram simulation, ground-truth acquisition, and the collection of training data under the slightly off-axis DH system in detail. We also discuss the FT phase recovery under different window sizes and show the DL-noPhy model. In addition, we showcase supplementary experiment results on a new group of live cells by three phase recovery methods (FT, VHQPI, and DL-VHQPI).

### Section 1: Low-carrier frequency hologram simulation and ground-truth acquisition

This section specifically introduces the simulation of low-carrier frequency holograms and the corresponding ground truth using MATLAB<sup>51</sup>. We select two images as intensity and phase of the object-light-wave complex amplitude ( $O(x, y)$ ), which can be written as

$$O(x, y) = A_o(x, y)\exp[i\varphi_o(x, y)] , \quad (S1)$$

where  $A_o(x, y)$  and  $\varphi_o(x, y)$  denote the intensity and phase distribution of the object-light wave, respectively. An aberration term  $Q(x, y)$  was added in the simulation because the object-light wave is inevitably affected by the aberration of the objective lens.

$$Q(x, y) = \exp(i(l_x x^2 + l_y y^2)) . \quad (S2)$$

The parameters  $l_x, l_y$  in Eq. (S2) describe the relative divergence between the object and reference beam caused by the mismatch in spherical phase curvature. We incorporated an aperture limit to the object-light wave to simulate the effect of the objective lens in the DH imaging system. The pupil function is expressed as

$$\text{circ}(u, v) = \begin{cases} 1 & \sqrt{u^2 + v^2} \leq NA/\lambda \\ 0 & \sqrt{u^2 + v^2} > NA/\lambda \end{cases} , \quad (S3)$$

where  $NA/\lambda$  is the effective cut-off frequency in the imaging system with the objective lens, and  $(u, v)$  is the coordinate of  $(x, y)$  corresponding to the spatial frequency domain (SFD). The complex amplitude distribution of the object-light wave passing through the objective lens system is described as

$$O_s(x, y) = \mathcal{F}^{-1}\{\mathcal{F}\{O(x, y)\} * \text{circ}(u, v)\} * Q(x, y) , \quad (S4)$$

where  $\mathcal{F}$  and  $\mathcal{F}^{-1}$  respectively denote Fourier transform and inverse Fourier transform operator, and “\*” denotes matrix multiplication. In the reference light arm shown in Figure S1(a), the plane wave field  $R(x, y)$  is propagated.

$$R(x, y) = A_R(x, y)\exp(i\varphi_R(x, y)) . \quad (S5)$$

We used a two-dimensional standard Gaussian distribution as the reference wave intensity to simulate environmental disturbance in the wavefront propagation.

$$A_R(x, y) = \frac{1}{2\pi} \exp\left(-\frac{x^2 + y^2}{2}\right) . \quad (S6)$$

Due to a slight angle between the object beam and the reference beam, a linear tilt component is imposed on the reference-wave phase distribution.

$$L(x, y) = \exp[i\varphi_R(x, y)] = \exp[i(k_x x + k_y y)] , \quad (S7)$$

where the factors  $k_x, k_y$  denote the linear phase difference between  $O_s(x, y)$  and  $R(x, y)$ . Tuning the  $k_x$  and  $k_y$  values can control the separation degree of the twin image in the SFD so that the simulated holograms can be adjusted into a slightly off-axis state.

Finally, we obtained the emulated low-carrier frequency hologram by solving the square of the modulus of the sum of the  $O_s(x, y)$  and  $R(x, y)$ . The intensity distribution of the hologram can be written as

$$I_H(x, y) = |O_s + R|^2 = |O_s|^2 + |R|^2 + O_s^* R + R^* O_s , \quad (S8)$$

Correspondingly, we can also get the ground truth (Background,  $I_{BG}(x, y)$ ) in numerical simulation by calculating the sum of the squares of the modulus values of the two ( $O_s(x, y)$  and  $R(x, y)$ ).

$$I_{BG}(x, y) = |O_s(x, y)|^2 + |R(x, y)|^2 , \quad (S9)$$

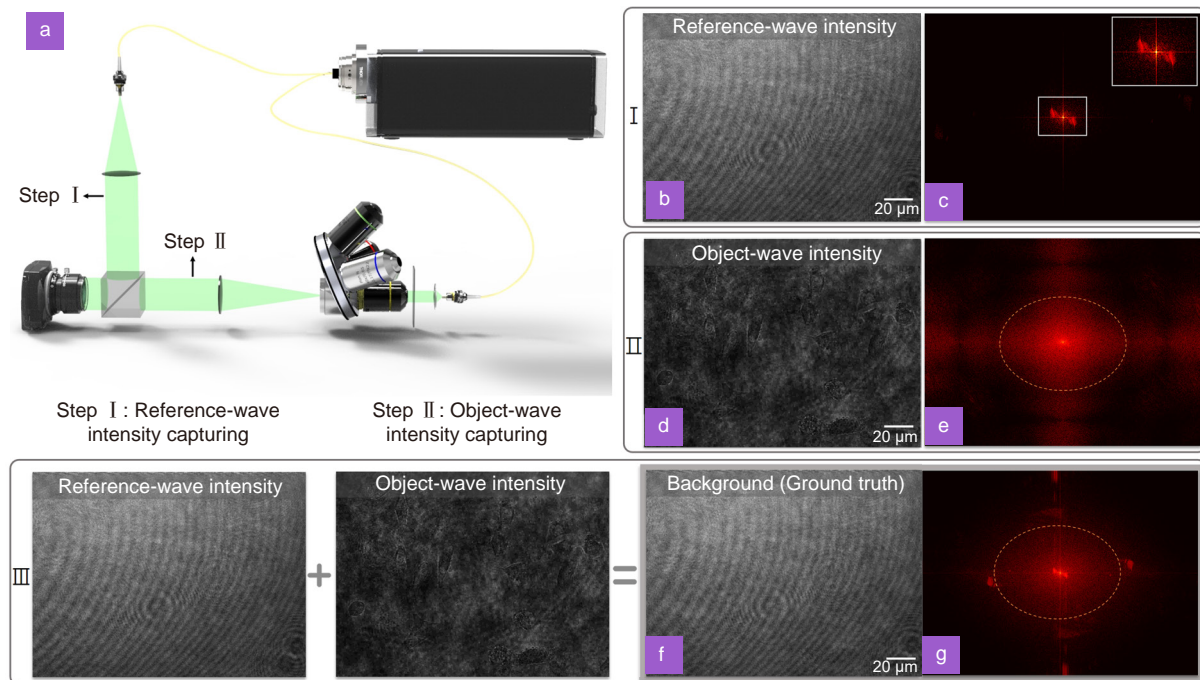


**Fig. S1 | The flow chart of ground-truth acquisition under a slightly off-axis system.** (a) Slightly off-axis interference optical path. (b) and (d) The captured reference-wave intensity and object-wave intensity. (c) and (e) The spatial frequency spectrum of (b) and (d). (f) and (g) The captured ground truth (background) and its spatial frequency spectrum. I, II, III are the three steps of ground-truth acquisition.

### Section 2: Collection of training data from slightly off-axis DH system

The low-carrier frequency fringe demodulation by the DL-VHQPI always needs the paired training data because the used DNN is a supervised learning model. However, it is difficult to obtain the ground truth through a single image acquisition in a slightly off-axis state due to the inevitable spectrum-overlapping of the autocorrelation and cross-correlation terms in the SFD. We set up the optical path structure as shown in Fig. S1(a), tuned it to a high-stable state, and obtained the ground truth (background) through the following three steps<sup>S2</sup>: 1) Collect the reference-wave intensity ( $A_R(x, y)$ ) by blocking the object-wave light path, as shown in Fig. S1(b). 2) Block the reference-wave light path to capture the object-wave intensity ( $A_O(x, y)$ ), as shown in Fig. S1(d). 3) Obtain the complete background term as ground truth by adding the two together according to Eq. (S9), and the detail can be seen in Fig. S1(III). Figure S1(c, e, g) also separately showcase the spectrum of reference wave, object wave, and background.

### Section 3: Discussion of FT phase recovery with different window sizes

When the FT method is used for low-carrier frequency fringe demodulation, the SFD filtering utilizing a filter window calculated from the theoretical numerical aperture (NA) will severely suffer from the impact of the autocorrelation term<sup>S3</sup>. Although reducing the size of the filter window can alleviate this effect to some extent, this comes at the expense of the system space bandwidth product (SBP) and imaging quality. Here, we discuss the FT phase recovery results for different window sizes and give quantitative analysis under numerical simulation. Figure S2(a) showcases SFD filtering under different window sizes (shown in Red, Yellow, and Blue). Figure S2(b, c, d) provide the corresponding phase recovery results under different filtering windows, respectively. Figure S2(e) is the ground truth. The cross-section analysis is shown in Fig. S2(f) demonstrates that reducing the filter window size indeed suppresses phase artifacts. Figure S2(g) quantitatively analyzes the phase reconstruction accuracy. The results demonstrate that reducing the FT filter window size not only sacrifices the SBP of the system but also causes a decrease in imaging accuracy due to the loss of high-frequency components caused by the limited filter window.

We further verified this issue in the live-cell experiment. Figure S3(a) illustrates spectrum filtering under different sizes shown in red and yellow filter windows. Figure S3(d) shows the FT phase recovery results with a smaller filter window. The phase artifacts indeed are suppressed, but the high-frequency information loss of the sample causes blurred

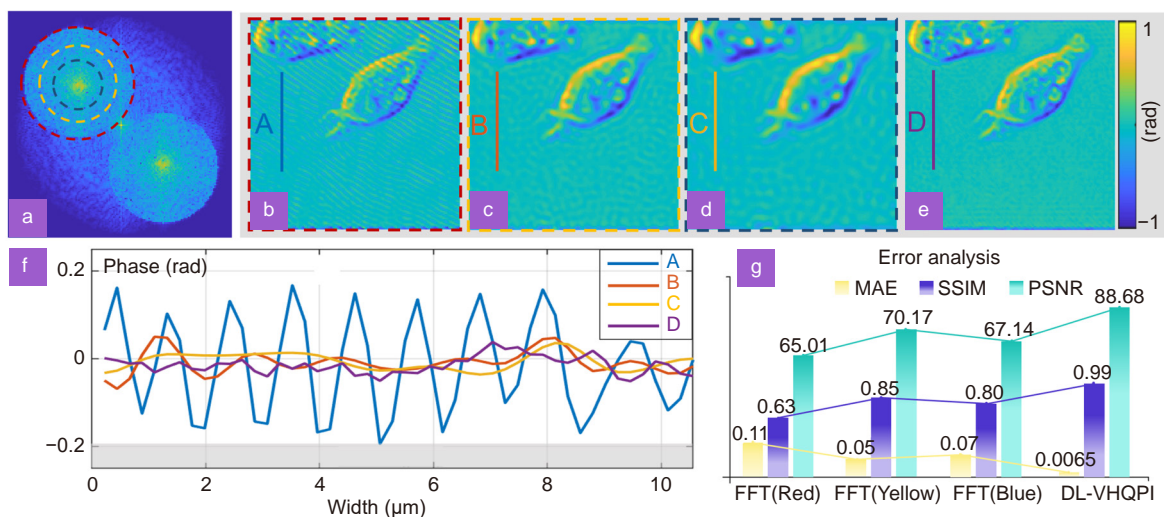


**Fig. S2 | The FT phase recovery results and quantitative analysis under different window sizes in numerical simulation. (a)** Spectrum filtering under different sizes, seen in red, yellow, and blue circle windows. **(b–d)** The reconstructed phase results based on the FT method under the three filtering windows. **(e)** The ground truth. **(f)** The cross-section of the background part in (b–e). **(g)** The phase error analysis.

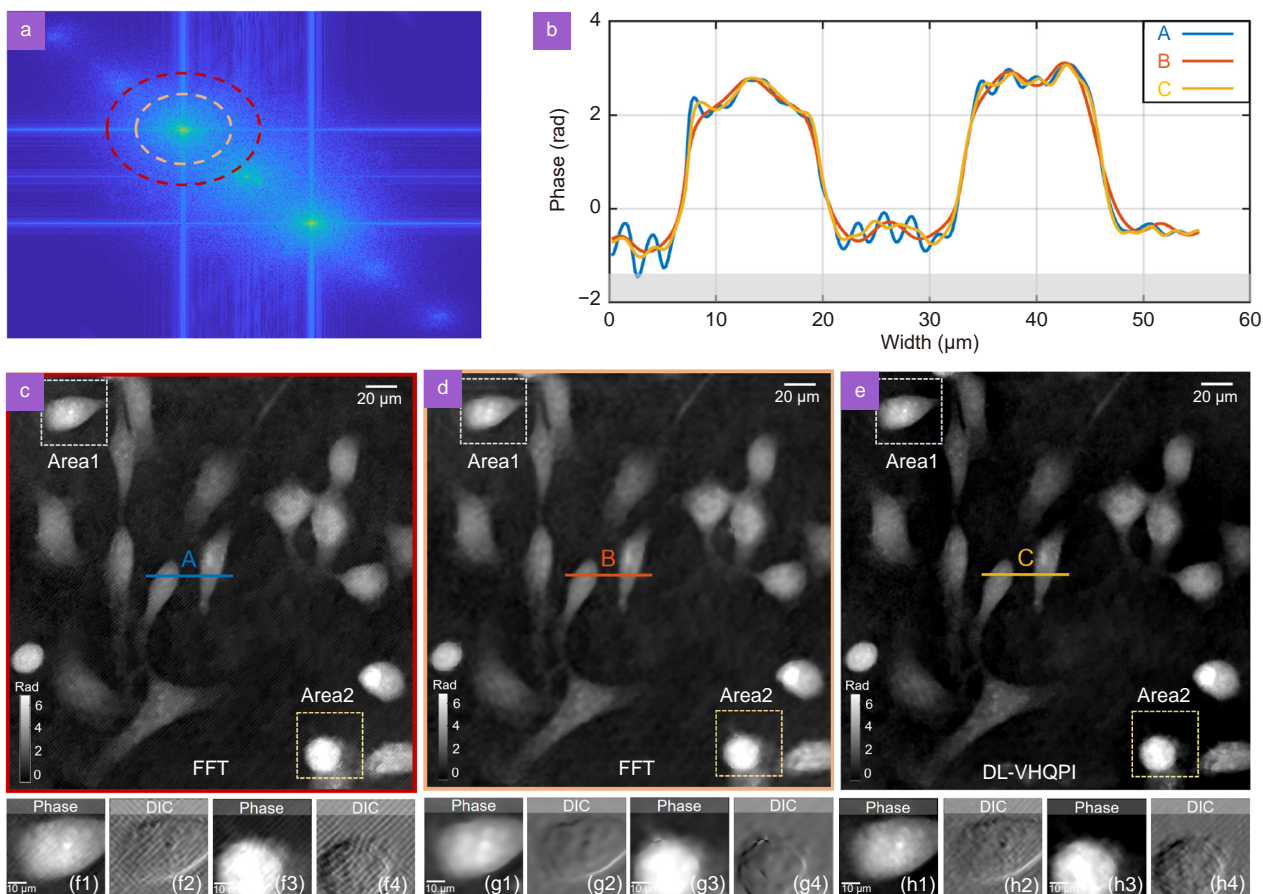


**Fig. S3 | The discussion of FT phase recovery results under different window sizes in the live-cell experiment. (a)** The different spectrum selections in FT phase recovery. **(b)** The cross-section analysis of (c–e). **(c)** and **(d)** The corresponding FT phase reconstructed results under red and yellow filter windows. **(e)** The result of DL-VHQPI. **(f1–f4)**, **(g1–g4)** and **(h1–h4)** The enlarged views and DIC views of the ROIs (Area1 and Area2).

imaging.

The cross-section shown in Fig. S3(b) also quantitatively demonstrates the artifacts-suppression effect by decreasing the size of the filter window. The results reconstructed under the filter window calculated by theoretical NA are shown in Fig. S3(c), and the spectrum-overlapping causes imaging artifacts to impair imaging quality; In comparison, the results recovered by DL-VHQPI can achieve high-accuracy artifacts-free imaging, as shown in Fig. S3(e). Figure S3(f1–f4), S3(g1–g4), and S3(h1–h4) show the magnified views and differential interference contrast (DIC) views of the regions of interest (ROI, Area1, and Area2), respectively. The FT phase reconstruction at smaller filter sizes sacrifices much of the high-frequency detail of the sample, causing non-ideal imaging results. Therefore, DL-VHQPI can not only suppress phase artifacts but also preserve high-frequency details of the specimens with great imaging quality.

#### Section 4: DL-noPhy network description

DL-noPhy uses the Convolution Neural Network (CNN), the same as the CNN1 in DL-VHQPI, which offers a more reasonable comparison with DL-VHQPI. The difference is that DL-noPhy uses the hologram as input and background as the ground truth for training without considering the residual compensation and physical processes. To be exact, DL-noPhy is an end-to-end neural network model that does not have a physic-prior like uVID in DL-VHQPI but directly “learns” the fringe pattern to the background through DNN. Obtaining a desired result under such a model often requires a massive dataset and powerful feature extraction capability. The specific network is shown in Fig. S4.

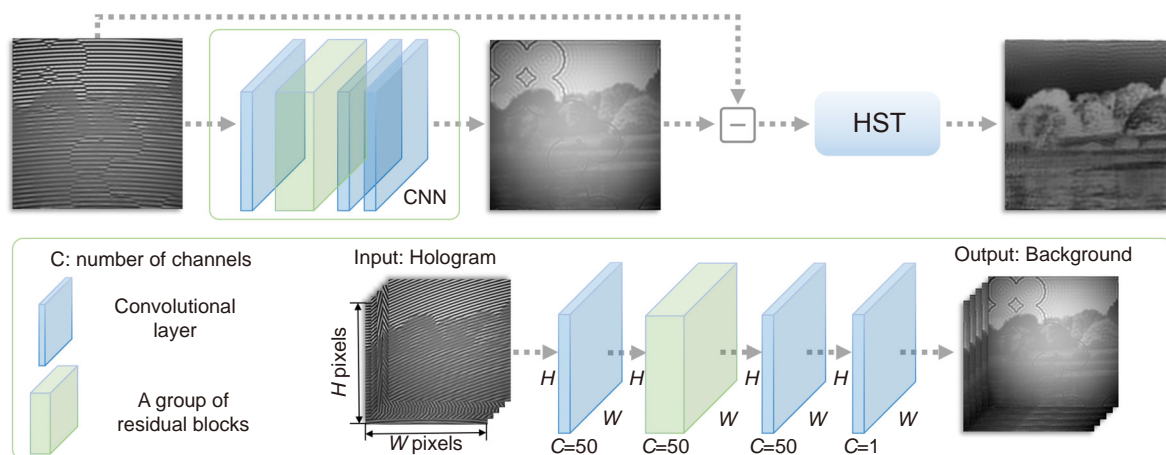
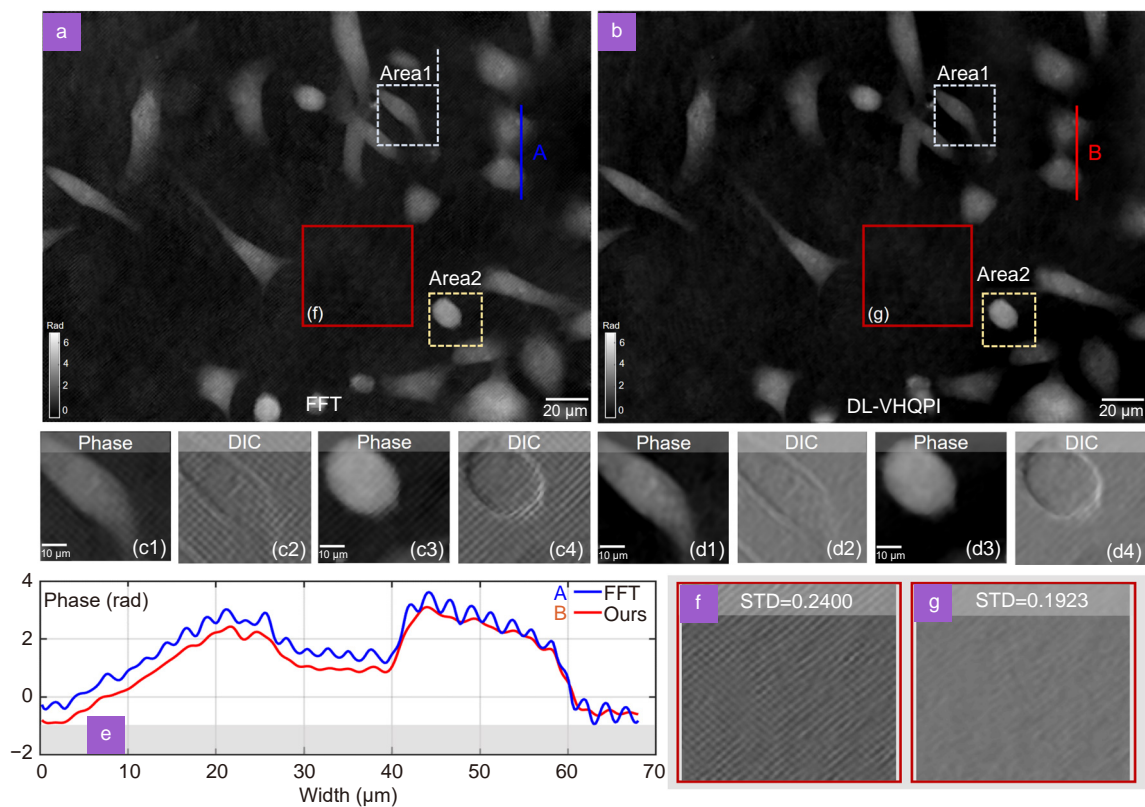


Fig. S4 | Network structure framework for the DL-noPhy approach.

#### Section 5: Supplementary experiment results based on FT and VHQPI methods for living cells

To further validate the effectiveness of phase recovery by DL-VHQPI for more samples, we added an experiment on a new group of cells, as shown in Fig. S5. Figure S5(a) and S5(b) respectively showcase the phase results using FT and DL-VHQPI. Two ROIs (Area1 and Area2) are selected to highlight the capability of artifacts suppression. Figure S5(c1, c3, d1, d3) are the enlarged views, and Figure S5(c2), S5(c4), S5(d2), and S5(d4) are their corresponding phase gradient images through digital DIC. The cross-section demonstrates that the fringe-like artifacts are well suppressed in DL-VHQPI results compared with FT results. The DIC views of the red rectangle in Fig. S5(a) and S5(b) are shown in Fig. S5(f) and S5(g), which showcase the artifacts-suppression effect on the phase background part. At the same time, the calculated Standard Deviation (STD) quantitatively demonstrates that DL-VHQPI enjoys a better flatness distribution.

Furthermore, we also carried out the VHQPI-based method comparison experiment<sup>S4,S5</sup>. The recovered results, as shown in Fig. S6(a), demonstrate that the frequency component extraction algorithm (uVID) can somewhat suppress phase artifacts. However, the magnified views of the phase details, as shown in Fig. S6(c1–c4), show that there are still phase artifacts caused by the non-sufficient background term removal. In contrast, the imaging result based on DL-VHQPI is superior to that obtained by the VHQPI, as shown in Fig. S6(b) and S6(d1–d4). However, it can be easily found that in the live-cell experiment, the imaging quality of DL-VHQPI is improved compared with that of VHQPI, but the improvement is within a certain limit due to the ground truth acquisition. Although we have tried to make the



**Fig. S5 | Supplementary results of the live-cell experiment.** (a) The phase recovery result based on the FT method. (b) The phase recovery result based on DL-VHQPI. (c1–c4) and (d1–d4) The magnified views of “Area1” and “Area2” for the two samples under different phase recovery methods. (c2, c4, d2, d4) The corresponding DIC views, respectively. (e) The numerical distribution of the cross-section. (f) and (g) The DIC views after partial magnification of the phase map in the corresponding red box.

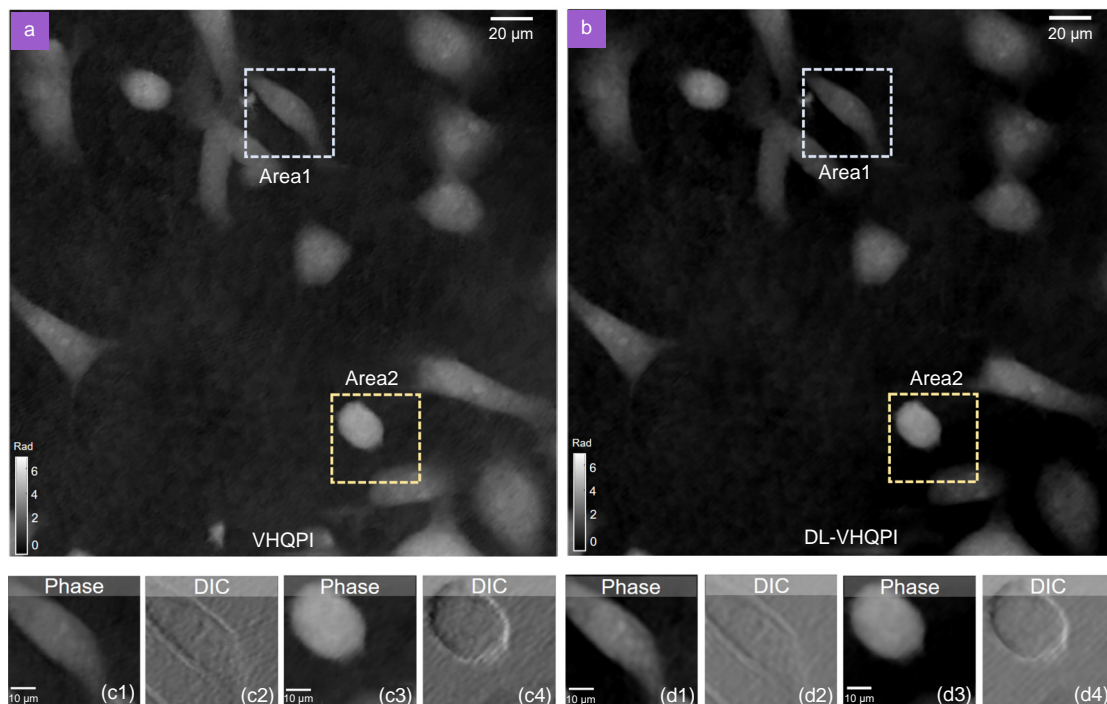


**Fig. S6 | Supplementary results of the live-cell experiment.** (a) The VHQPI method recovery results. (b) DL-VHQPI phase recovery results. (c1–c4) and (d1–d4) The magnified views of “Area1” and “Area2” for the two samples under the two phase recovery methods. (c2, c4, d2, d4) The corresponding DIC views, respectively.

optical path as stable as possible in our experiments, it is still difficult to obtain reliable ground truth because of the inevitable environmental disturbances and the system-inherent instability. We will continue to solve this issue in our future work.

## References

- S1. Baek Y, Lee K, Shin S, Park Y. Kramers–Kronig holographic imaging for high-space-bandwidth product. *Optica* **6**, 45–51 (2019).
- S2. Fan Y, Li JJ, Lu LP, Sun JS, Hu Y et al. Smart computational light microscopes (SCLMs) of smart computational imaging laboratory (SCILab). *Photonix* **2**, 19 (2021).
- S3. Li ZS, Fan Y, Sun JS, Zuo C, Chen Q. A commercialized digital holographic microscope with complete software supporting. *Proc SPIE* **11571**, 115711C (2020).
- S4. Trusiak M, Cywińska M, Micó V, Picazo-Bueno JÁ, Zuo C et al. Variational Hilbert quantitative phase imaging. *Sci Rep* **10**, 13955 (2020).
- S5. Cywińska M, Trusiak M, Patorski K. Automatized fringe pattern preprocessing using unsupervised variational image decomposition. *Opt Express* **27**, 22542–22562 (2019).